

## Effect of electropulsing on deformation behavior of Ti–6Al–4V alloy during cold drawing

Yan ZHOU, Guo-qing CHEN, Xue-song FU, Wen-long ZHOU

School of Materials Science and Engineering, Dalian University of Technology, Dalian 116085, China

Received 8 May 2013; accepted 9 August 2013

**Abstract:** Electron backscattered diffraction (EBSD) and transmission electron microscopy (TEM) were used to investigate effect of electropulsing on microstructure and texture evolution of Ti–6Al–4V during cold drawing. Research results demonstrate that the electropulsing treatment (EPT) can enhance the deformability of the grains with unfavorable orientations, which makes the compatibility of deformation among grains much better. A comparison in texture evolution between conventional cold drawing and EPT cold drawing indicates that the EPT promotes prismatic  $\langle a \rangle$  slip moving, restricts pyramidal  $\langle c+a \rangle$  slip occurring and accommodates the deformation with  $c$ -component by grain boundary sliding. The fraction decrease of low-angle grain boundaries for samples deformed with EPT reveals that the application of electropulsing restricts the formation of the incidental dislocation boundaries and the geometrically necessary boundaries.

**Key words:** Ti–6Al–4V alloy; electropulsing; cold drawing; texture evolution

### 1 Introduction

Titanium alloys are prominent materials applied in the aerospace, energy, and biological industry because of their excellent characteristics, such as the combination of low density with high strength, good corrosion resistance, and high-temperature performance [1,2]. Ti–6Al–4V alloy is the most commonly used titanium alloy [3]. Because of its HCP crystal structure, the deformability of Ti–6Al–4V alloy is low at room temperature [4]. As a result, the alloy has to be deformed at elevated temperature during the rods, pipes, and wire production. Hot working conditions need high-level equipment and complex processes. Moreover, Ti–6Al–4V alloy would likely react with oxygen at high temperature, leading to the instability of product quality. Therefore, it is important for Ti–6Al–4V alloy to deform at lower temperature. This attempt needs systematically investigation on the deformation behavior of the material under different deformation conditions. In the past, a good number of studies have focused on the factors, such as strain rate [5], reduction [6], chemical composition [7], and original orientation of grains [8], which could influence the deformation behavior of titanium alloys at

room temperature. However, such factors are uncontrollable or little effective on Ti–6Al–4V alloy.

Recently, several studies have found that high-density electropulsing can reduce the flow stress and improve the properties of the materials. CONRAD and YANG [9] systematically studied the deformation behavior of fine-grained MgO under the electric field. The electric field can decrease the flow stress and increase the elongation of the material. The same conclusion was also derived in the research of plastic deformation kinetics of electrodeposited Cu under the electric field [10]. CONRAD [11] predicted that the reduction of flow stress resulted from the influence of an electron wind produced by the electric field at the pre-exponential of the thermally activated motion equation of dislocations.

Extensive investigation on the microstructure and texture evolution of the materials deformed under electropulsing treatment (EPT) is important for the application of electroplastic deformation technique. In the present, several studies focus on the microstructure evolution combined with the recrystallization mechanism during the electroplastic deformation processes or electric field annealing. GUAN et al [12] studied the recrystallization behavior of cold rolling AZ31

magnesium alloy with EPT. HE et al [13] studied the effects of electric field annealing on the development of recrystallization texture and microstructure in cold-rolled interstitial-free steel. For the application of electropulsing to titanium alloys, several researches were carried out on the recrystallization behavior and grain refinement induced by the EPT [14,15]. Such studies were performed at high temperature caused by Joule heat brought from large electropulsing current. However, the influence of electropulsing on the deformation mechanism of titanium alloys at a relatively low temperature was not reported.

In this work, the microstructure and the texture evolution of Ti–6Al–4V alloy during conventional cold drawing and EPT cold drawing were systematically studied. The effects of electropulsing on the deformation mechanism of the materials were investigated by electron backscattered diffraction (EBSD) and transmission electron microscopy (TEM).

## 2 Experimental

The as-received Ti–6Al–4V wire (3.5 mm in diameter), which had a hot drawing history with chemical composition shown in Table 1, was annealed at 820 °C for 2 h, and then cooled in the furnace to stabilize the microstructure and remove residual stresses. Oxide coating was cleared away before the EPT cold drawing experiment, and the wire was straightened to maintain perfect contact with the electrode. The wires were cold-drawn with two passes: with and without EPT. The reduction per pass was 20%, as defined in the following equation:

$$\varepsilon = 2 \ln(D_0/D_1) \quad (1)$$

where  $\varepsilon$  is the deformation reduction;  $D_0$  and  $D_1$  are the diameters before and after cold drawing, respectively.

**Table 1** Chemical composition of as-received Ti–6Al–4V wire (mass fraction, %)

Al	V	Fe	Si	Ti
6.0112	4.0038	0.1695	0.0742	Bal.

The experiment was carried out at room temperature. The arrangement of the electropulsing cold-drawing process is illustrated schematically in Fig. 1. The Ti–6Al–4V wire took approximately 920 ms to move from positive electrode to the drawing die at a speed of 0.05 m/s. Then, the deformed material was immediately oil-cooled to stabilize the microstructure after the EPT cold drawing. The Hall effect sensor connected to the digital storage oscilloscope was used to detect the electropulsing waveform. It was triangular wave (see Fig. 2) with a maximum current density of 241 A/mm<sup>2</sup>,

duration of 40  $\mu$ m, and frequency of 200 Hz. The drawing direction was same to the electric current flow.

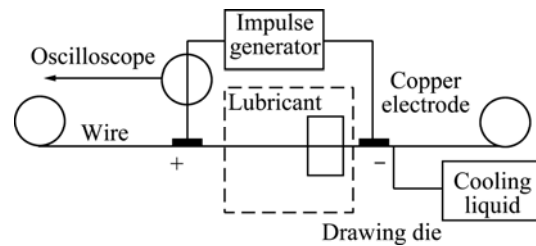


**Fig. 1** Schematic diagram of experimental arrangement for EPT cold drawing

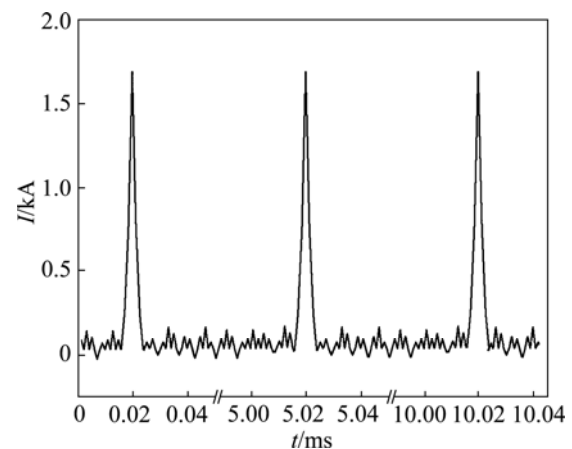


**Fig. 2** Typical waveform of electropulsing

Strength properties of deformed wires were determined by MTS828 test machine at the tensile rate of 6 mm/min. EBSD analyses were performed on a JEOL JSM–7001F scanning electron microscope at 20 kV to study the microstructure and texture evolution of  $\alpha$  phase. Specimens were cut along their drawing axes and prepared by mechanical grinding using emery paper with different particle sizes from 0.075 to 0.012 mm. The specimens were then electropolished in a solution of 50 mL perchloric acid and 950 mL glacial acetic acid at 30 V for 30 s. Data analysis was performed using the TSL OIM software. A step size of 0.5  $\mu$ m for all the samples was chosen to capture an area of 90  $\mu$ m $\times$ 75  $\mu$ m taken from the central part of the longitudinal section. Secondary electron images were obtained to study the morphology changes of the  $\beta$  phase. The specimens were initially etched using a reagent containing 2 mL hydrofluoric acid, 4 mL nitric acid and 94 mL water for 15 s. Thin foils were prepared from the longitudinal plane of the deformed material for TEM investigation. The specimens were mechanically polished and thinned using a Tenupol–5 twin-jet electrolytic polisher in a solution containing 6% perchloric acid, 35% butyl alcohol, and 59% methanol (volume fraction) at –30 °C. The prepared foils were examined using a Tecnai G<sup>2</sup>20 transmission electron microscope operated at 200 kV.

### 3 Results

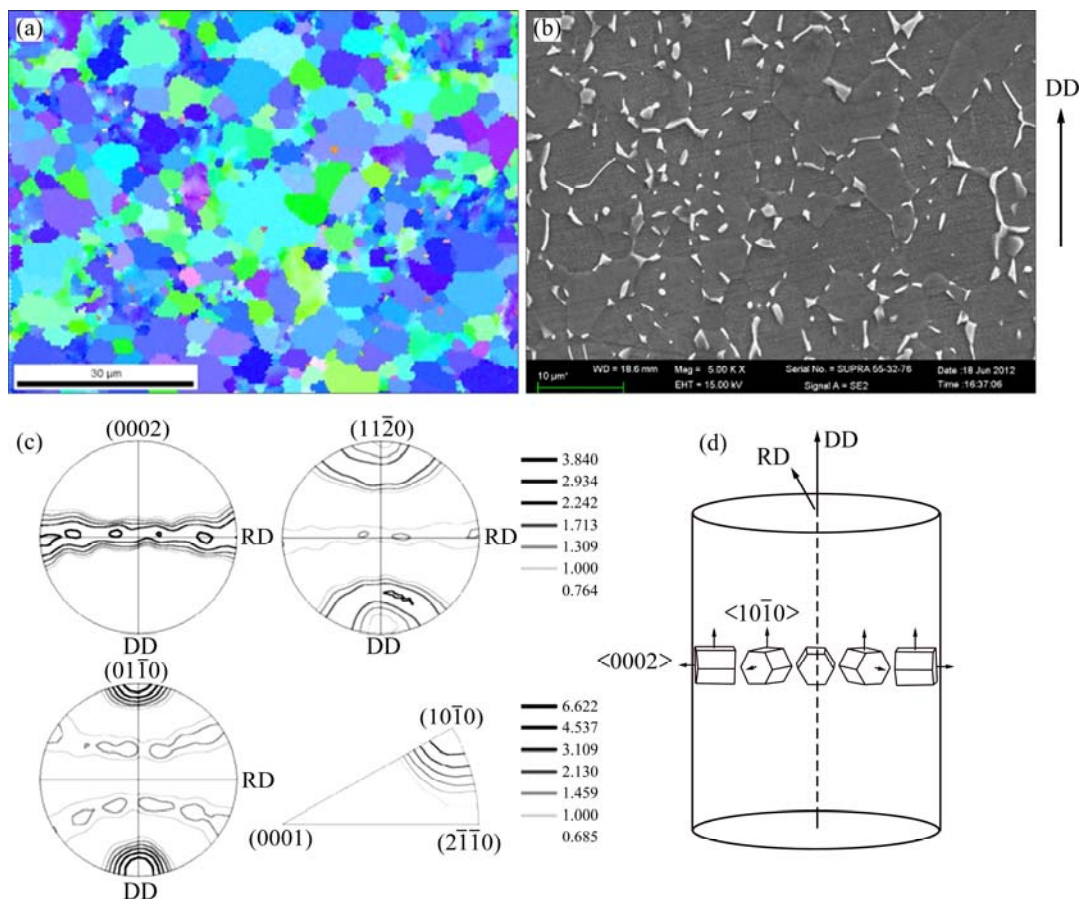
#### 3.1 Initial texture and microstructure

Figure 3(a) shows the EBSD image of the starting material in drawing direction (DD), showing the crystal orientation distribution of  $\alpha$  phase grains by different colors. The red is for  $\langle 0001 \rangle$  parallel to DD, the green is for  $\langle 11\bar{2}0 \rangle$ , and the blue is for  $\langle 10\bar{1}0 \rangle$ . It can be seen that  $\langle 10\bar{1}0 \rangle$  grains dominate in the image. The absence of red grains indicates that the  $\langle 0001 \rangle$  does not lie along DD. The (0002) pole figure in Fig. 3(c) demonstrates that (0002) is almost parallel to the drawing direction, where a band is perpendicular to DD. The  $\langle 11\bar{2}0 \rangle$  pole figure shows a clustering of  $\langle 11\bar{2}0 \rangle$  perpendicular to DD, which is in accordance with the appearance of green grains in Fig. 3(a). The EBSD image and the (0002) pole figure indicate that the starting material has a strong basal texture. Evidently, basal slip systems are mostly activated during the hot drawing process and the texture is preserved. The  $\langle 10\bar{1}0 \rangle$  pole figure reveals that  $\langle 10\bar{1}0 \rangle$  is perpendicular to DD. In addition, the two

bands distributed symmetrically around DD are resulted from the flank prismatic plane of the material. Furthermore, a clustering of orientations located at  $\langle 10\bar{1}0 \rangle$  in the DD-inverse pole figure indicates that the starting material has a strong  $\langle 10\bar{1}0 \rangle$  fiber texture with respect to DD. This kind of fiber texture always appears in wrought titanium and its alloys after the drawing and extrusion deformation [6,16]. In the EBSD image, only  $\alpha$  phase can be observed and no  $\beta$  phase appears. But the  $\beta$  phase arises obviously in the secondary electron image (Fig. 3(b)). This is because the step size of the EBSD analysis is larger than that of the  $\beta$  phase size. In this work, the  $\alpha$  phase deformation behavior was mainly discussed.

#### 3.2 Mechanical properties

Figure 4 shows the true stress–strain curves of the wires deformed with or without EPT. The strength of the wire deformed with EPT is 42 MPa lower than that without EPT. However, the elongation is enhanced obviously. This result indicates that the electropulsing can increase the deformation ability of Ti–6Al–4V alloy.



**Fig. 3** Microstructure and texture of as-received Ti–6Al–4V wire revealed by EBSD and secondary electron images in longitudinal plane: (a) EBSD generated microstructure (inverse pole figure map of DD axis); (b) Secondary electron image of starting material; (c) Pole figures and DD-inverse pole figure of initial texture (Gray color bars represent texture intensity); (d) Dominating texture components revealed by EBSD

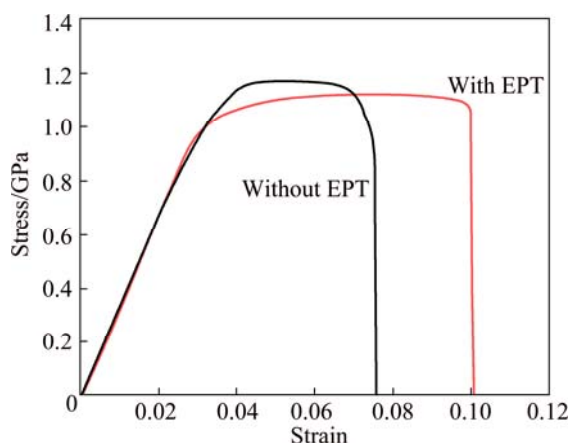


**Fig. 4** Comparison of stress–strain curves of Ti–6Al–4V wires deformed with or without EPT

### 3.3 Microstructure evolution

Figure 5 shows the EBSD images of Ti–6Al–4V wire at 40% reduction by conventional cold drawing and EPT cold drawing. The investigated areas were taken from the central part of the longitudinal plane. The figures show that the grains of  $\alpha$  phase are elongated along DD in the two specimens, indicating that the dislocation slip is the main deformation mechanism [16]. Moreover, severe plastic deformation results in the effective grain size refinement. The TSL OIM software was used to detect the grain size reducing from the initial value of  $4.07\ \mu\text{m}$  to  $2.63\ \mu\text{m}$  and  $1.79\ \mu\text{m}$  after deformation with or without EPT, respectively. Neither the average grain size nor the morphology of the grains shows significant difference in the two images shown in Fig. 5. But the color-coded grain distribution indicates that the texture evolution is different in the two specimens. In comparison, the proportion of  $\langle 11\bar{2}0 \rangle$  grains in the specimen after EPT cold drawing is much larger than that by conventional cold drawing.

The magnified image of Fig. 6 captured from the local area Fig. 5(a) demonstrates the existence of twins. The occurrence of twins indicates that the coordinated deformability is not good during conventional cold drawing. TSL OIM analysis reveals that the twin is extension twin and its misorientation angle is  $85^\circ$ . The twin deformation mechanism is very difficult to nucleate in Ti–6Al–4V alloy [8]. The occurrence of twin phenomenon demonstrates that strain hardening during conventional cold drawing is strong, explaining why the strength of the wire deformed without EPT is higher than that with EPT.

Figure 7 shows the secondary electron images of two specimens with different cold drawing processes. After 40% deformation, the  $\beta$  phase of both specimens is restricted at the boundaries and straightened along the DD with the deformation of  $\alpha$  grains. Figure 7(a) shows

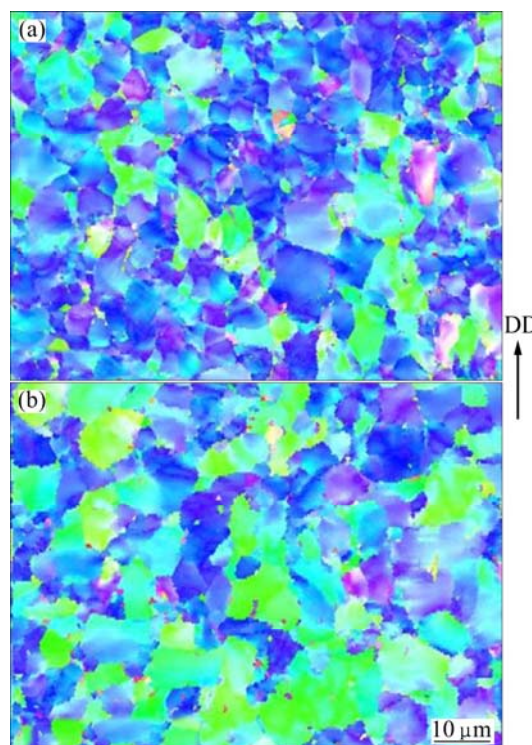


**Fig. 5** EBSD images of Ti–6Al–4V wire after cold drawing to 40% reduction along DD: (a) Conventional cold drawing; (b) EPT cold drawing

that the deformation of  $\beta$  phase is inhomogeneous evidently. Some  $\beta$  phase grains are elongated along the DD, while others are still restricted to the triple points among  $\alpha$  grains. This phenomenon implies that inhomogeneous deformation also exists for  $\alpha$  phase grains due to the plastic anisotropy of  $\alpha$  grains. Moreover, some  $\beta$  phase morphologies are bent along the triple grain boundary to coordinate the deformation anisotropy of  $\alpha$  phase grains.

Figure 8(a) shows that the dislocation cell can be observed by TEM in the deformed material without EPT. The appearance of the dislocation cell indicates that the cross slip is activated due to severe lattice friction. In comparison, the dislocation density in the specimen deformed by electropulsing is evidently lower than that without EPT, as shown in Fig. 8. After deformation with EPT, the long and straight prismatic  $\langle a \rangle$  dislocation with edge character appears around the grain boundary, as seen in Fig. 8(b).

### 3.4 Texture evolution

The inverse pole figures of DD for the EBSD images of Figs. 5(a) and (b) are presented in Fig. 9. The original material exhibits high intensity of DD with respect to  $\langle 10\bar{1}0 \rangle$ , as shown in Fig. 3(c). After 40% deformation, the type of texture does not change for both specimens, but the intensity decreases compared with the original texture (see Figs. 9(a) and (b)). Moreover, the

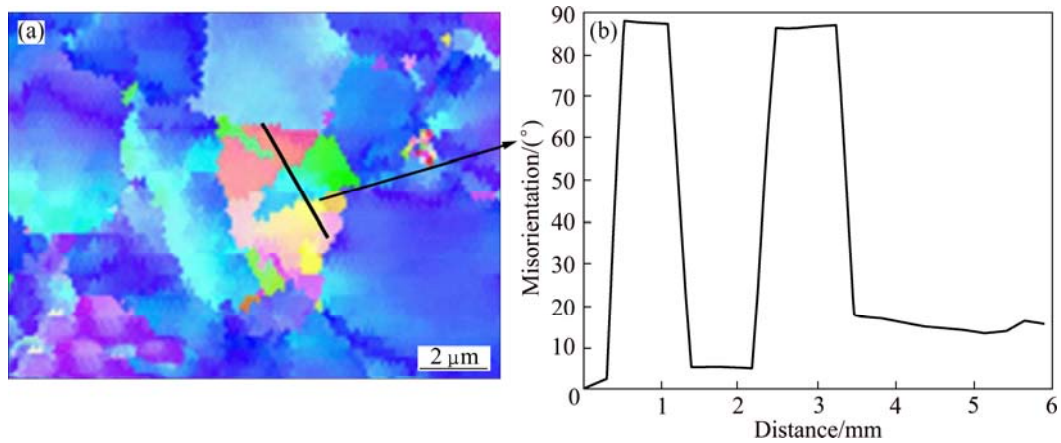


Fig. 6 Magnified EBSD image (a) and misorientation (b) of tension twinning appearing in conventional cold drawing

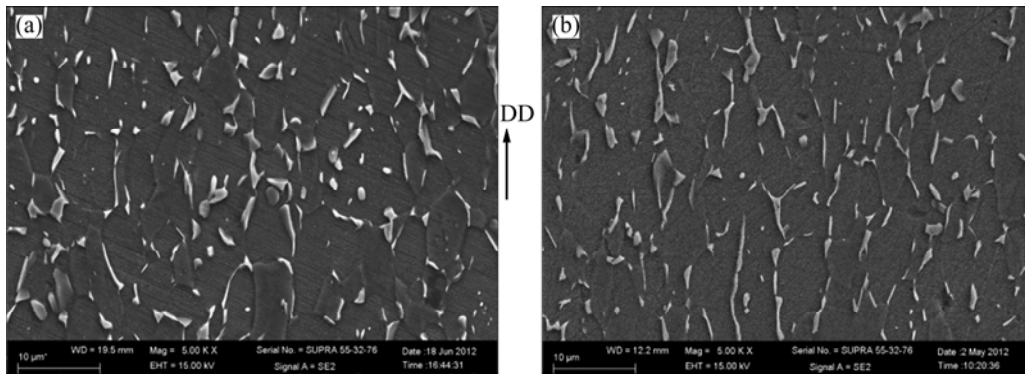


Fig. 7 Secondary electron images of Ti-6Al-4V wire after cold drawing at 40% reduction: (a) Conventional cold drawing; (b) EPT cold drawing

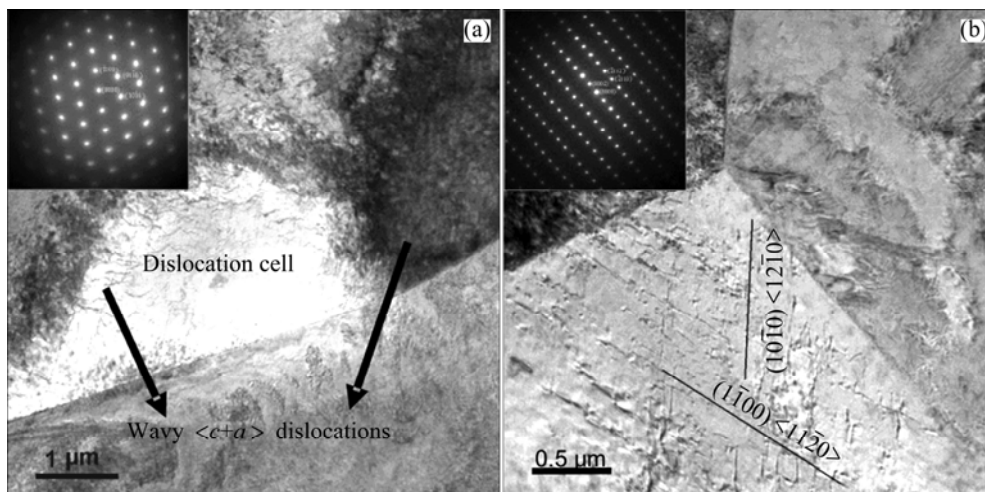


Fig. 8 Bright-field TEM images of deformed specimens: (a) Details of dislocation cell in specimen after conventional cold drawing; (b) Long and straight  $\langle a \rangle$  dislocations in specimen after EPT cold drawing

intensity of DD tends to rotate from  $\langle 10\bar{1}0 \rangle$  to  $\langle 11\bar{2}0 \rangle$  in both samples during the deformation. And the rotation tendency is greater in the EPT cold drawing sample. In addition, careful comparison between Figs. 9(a) and (b), conventional cold drawing sample has  $8^\circ$  rotation at the outer rim of the unit orientation triangle towards  $\langle 0001 \rangle$ , as seen in Fig. 9(c).

### 3.5 Evolution of grain boundaries

Utilizing the TSL OIM software supplied with the EBSD equipment, a systematic analysis of the boundaries was implemented. The misorientation angles and their characteristic distributions were also examined in this work.

#### 3.5.1 Misorientation angle evolution

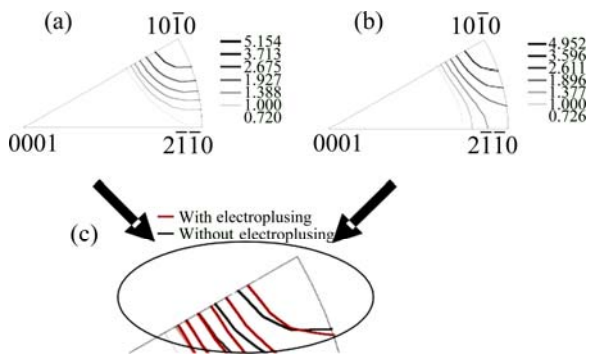


**Fig. 9** Inverse pole figures of DD for EBSD images of Figs. 5(a) and (b): (a) Conventional cold drawing; (b) EPT cold drawing; (c) Comparison between Figs. 9(a) and (b)

The microstructures of grain-boundary in Figs. 5(a) and (b) are given in Fig. 10, where low-angle boundaries (LAGBs) are represented by red lines, mid-angle boundaries (from  $5^\circ$  to  $15^\circ$ ) are represented by green lines, and high-angle boundaries (HAGBs) are represented by blue lines. A comparison between the two images shows that the fraction of LAGBs in the EPT cold drawing material is lower than that of conventional cold drawing by 3.4%. Numerous deformation-induced boundaries (DIBs) form in original grains of the deformed specimens because of severe plastic deformation, leading to effective grain fragmentation. By contrast, the EPT cold drawing process makes the sample have better deformation coordination such that the formation of DIBs is restricted.

Further investigation about in-grain misorientation evolution was determined, as shown in Fig. 11. The investigated areas were randomly selected coarse grains from Figs. 5(a) and (b). The selected grains were examined along the lines marked as *L1* and *L2* for the two samples. Each line passes through a whole grain from one side to the other side. For each measured line, the point-to-point (Fig. 11(c)) and point-to-origin (Fig. 11(d)) misorientations are given as a result. In

Fig. 11(c), the point-to-point misorientations of the EPT cold drawing *L2* are steadily below  $2^\circ$ , which approaches the detected precision of EBSD. However, point-to-point misorientations of conventional cold drawing *L1* have numerous peaks, indicating that several sub-boundaries generate. For the point-to-origin misorientations, the EPT cold drawing *L2* shows slow rising trend statistics in Fig. 11(d), which indicates that the dislocation of the deformed material under electropulsing has lower density and homogeneous distribution in the grains.

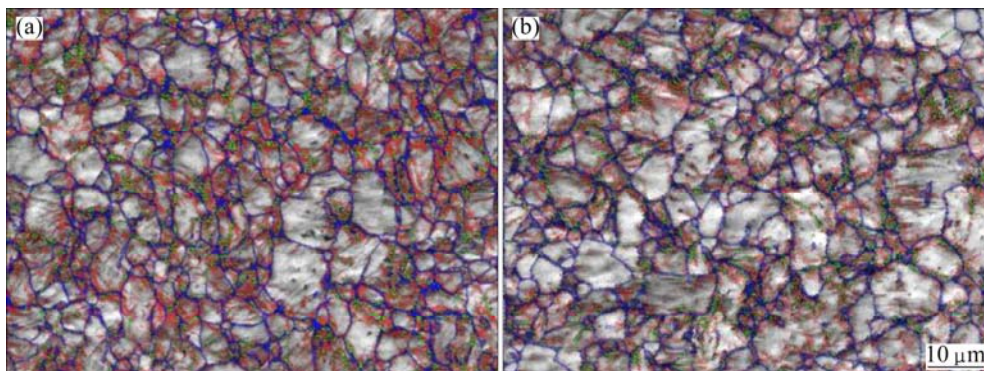
### 3.5.2 Misorientation axis distribution

Figure 12 shows the inverse pole figures that summarize the misorientation axis of the DIBs developed during the two different deformation processes. The misorientation axis distribution demonstrates strong intensity at  $\langle 0001 \rangle$  in both specimens. This type of distribution is attributed to the predominant activation of prismatic  $\langle a \rangle$  slip in Ti-6Al-4V alloy. In comparison between Figs. 12(a) and (b), the difference in misorientation axis distributions is pronounced. For conventional cold drawing specimen (Fig. 12(a)), several highly distinct maxima are present in the unit orientation triangle, such as the two peaks at  $\langle uvw0 \rangle$  in the angle range of  $20^\circ$ – $30^\circ$  and a clustering of axes close to  $\langle 2\bar{1}\bar{1}0 \rangle$  in the angle range of  $30^\circ$ – $40^\circ$ . These distribution types are absent in the specimen after EPT cold drawing (Fig. 12(b)).

## 4 Discussion

Previous studies showed that electropulsing significantly influenced the microstructure and texture evolution of materials. However, the theory regarding the phenomenon is not very clear up to now because of the confusion from the Joule heating effect produced by electropulsing.

During the experiment, the temperature rise ( $\Delta T$ ) can be considered an adiabatic process because of the short EPT time (only 920 ms), which can be calculated



**Fig. 10** Grain-boundary maps corresponding to different drawing conditions (lines with different colors represent grain-boundaries with different angles, red lines ( $2^\circ$ – $5^\circ$ ), green lines ( $5^\circ$ – $15^\circ$ ), blue lines (larger than  $15^\circ$ ): (a) Conventional cold drawing; (b) EPT cold drawing

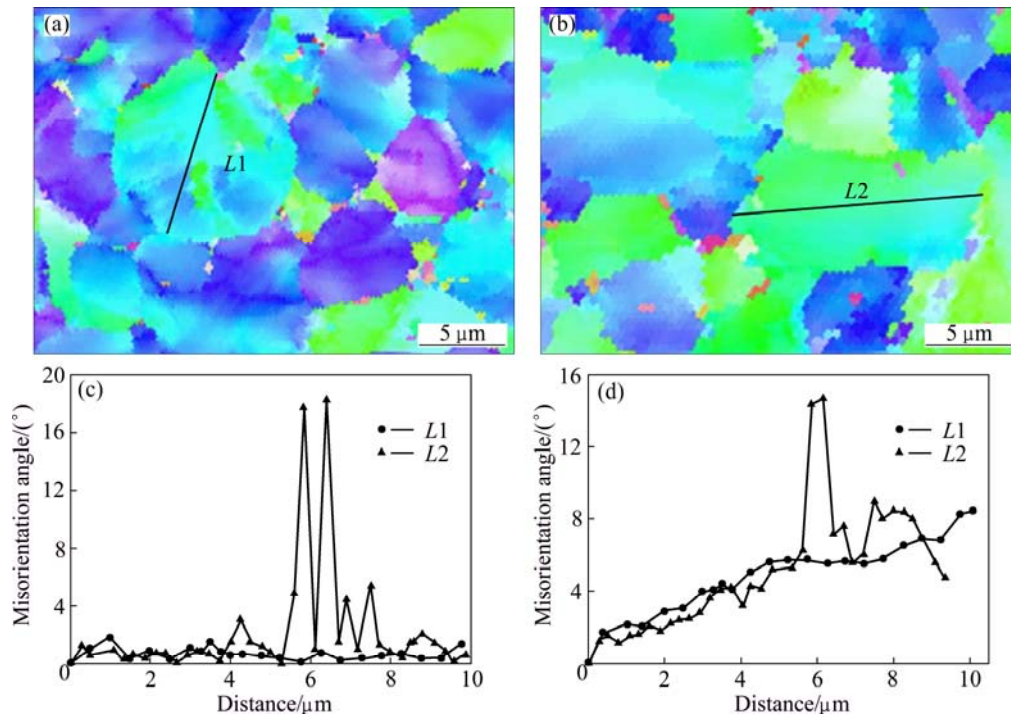


**Fig. 11** Details of EBSD images in Figs. 5(a) and (b) showing lines L1 (a) and L2 (b) for misorientation measurements and point-to-point (c) and point-to-origin (d) misorientation along lines L1 and L2

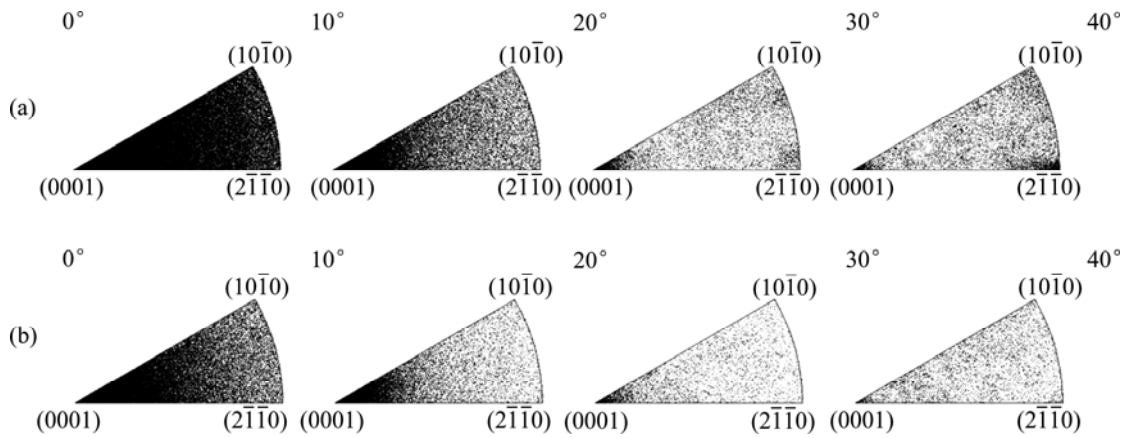


**Fig. 12** Misorientation (rotation)-axis distribution of deformed Ti-6Al-4V alloy after cold drawing at 40% reduction: (a) Conventional cold drawing; (b) EPT cold drawing

as [14,17]

$$\Delta T = (c\rho S^2)^{-1} \int_0^{t_p} \gamma J^2 dt \quad (2)$$

where  $J$  is the current intensity of the electropulsing (a function of  $t$ );  $t$  is the time of electropulsing treatment (920 ms);  $S$  is the cross sectional area of the specimen;  $\gamma$  is the electrical resistivity of Ti-6Al-4V alloy ( $1.8 \mu\Omega\cdot m$ );  $\rho$  is the density ( $4.44 \times 10^3 \text{ kg/m}^3$ ), and  $c$  is the specific heat capacity ( $750 \text{ J/(kg}\cdot^\circ\text{C)}$ ) of the specimen [14].

According to Eq. (2), in this work, the temperature rises due to the Joule heating effect during the first and second passes in cold drawing with EPT are 68 and

83 °C, respectively. The temperatures are much lower than the recrystallization temperature. The observed microstructure and texture evolution are significantly different between the conventional cold drawing and EPT cold drawing, indicating that high-density electropulsing is highly effective on the deformation behavior of Ti-6Al-4V alloy.

#### 4.1 Influence on microstructure evolution

The initial microstructure subjected to severe cold drawing deformation with 40% reduction changes dramatically. The secondary electron images show that the specimen by EPT cold drawing has better

deformation coordination as the morphology of  $\beta$  phase is slender and distributes homogeneously along the boundaries, as shown in Fig. 5. The distribution of  $\beta$  phase indicates that  $\alpha$  grains have good deformability because of the activation of unfavorable orientation by electropulsing.

A small amount of twins detected from the conventional cold drawing specimen implies the occurrence of severe inhomogeneous deformation. This type of deformation mechanism is considered to be difficult to perform in Ti–6Al–4V alloy. Twinning deformation has a strong influence on the strain hardening of materials [8]. The absence of twinning in specimen by EPT cold drawing (Fig. 5(b)) indicates that electropulsing improves the deformability of Ti–6Al–4V in cold drawing.

#### 4.2 Influence on texture evolution

The typical texture evolution of the material after EPT cold drawing in Fig. 9(b) shows that the intensity of DD is effectively rotated from the oriental  $\langle 10\bar{1}0 \rangle$  to  $\langle 11\bar{2}0 \rangle$ . AGNEW et al [18] suggested that the rotation was caused by prismatic  $\langle a \rangle$  slip in HCP materials. The rotation at the outer rim of the unit orientation triangle from  $\langle 10\bar{1}0 \rangle$  to  $\langle 0001 \rangle$  direction is restricted in the EPT cold drawing, which is different from conventional cold drawing where the  $c$ -axis rotates towards the loading direction due to the pyramidal  $\langle c+a \rangle$  slip [3]. Therefore, in the EPT cold drawing the electropulsing can restrict the activation of pyramidal  $\langle c+a \rangle$  slip. This result is in accordance with the report of GUBICZA et al [19] who suggested that the  $\langle c+a \rangle$  dislocations were immediately annihilated by electropulsing as a result of larger Burgers vector and higher formation energy than other dislocation types.

According to the von Mises law, five independent slip systems must be activated during the polycrystalline plastic deformation. However, prismatic  $\langle a \rangle$  slip can only provide two independent slip systems. Prismatic  $\langle a \rangle$  slip is the main deformation mechanism combined with “secondary” mechanisms to accommodate the deformation of  $c$ -components in titanium and its alloys [3,7,20]. The Schmid factor of the basal slip is smaller than 0.15 due to the strong basal texture in the original Ti–6Al–4V wires. Accordingly, basal slip is less activated in the specimens. During conventional cold drawing,  $c$ -component deformation is accommodated by pyramidal  $\langle c+a \rangle$  slip, which can provide four independent slip systems. However, pyramidal  $\langle c+a \rangle$  slip is restricted in the specimen deformed with EPT. Under these conditions, problems arise that the appropriate “secondary” mechanism needs to be provided. Several studies investigated the influence of electropulsing on the diffusion behavior and the grain boundary sliding in the

materials [20–22]. The electropulsing can influence the vacancy concentration and the diffusion coefficient of the materials. Moreover, grain boundary with high resistivity caused by large vacancy concentrations will generate greater Joule heat than that in the interior by electropulsing. This would impel faster diffusion along the grain boundary. Thus, grain boundary sliding is the appropriate “secondary” mechanism.

#### 4.3 Influence on grain boundary evolution

Severe plastic deformation is always accompanied by the development of DIBs. There are two type of DIBs according to their formation mechanism. One type of DIBs is derived from the accumulated dislocations at the grain boundaries due to severe lattice friction during the plastic deformation. The accumulated dislocations result in the cross slip of dislocation and further cause the formation of a dislocation cell (Fig. 8(a)). The ordinary cell boundary angle grows by merging with dislocations, and finally LAGBs form. This type of DIBs is called the incidental dislocation boundaries (IDBs). IDBs arise from the interaction of dislocations, and the fraction of IDBs reflects the dislocation pile-up degree. The other type of DIBs is called the geometrically necessary boundaries (GNBs), which is caused by different activities of slip systems at different parts of a grain. The stress state of different parts of a grain varies during severe plastic deformation because of the deformation anisotropy of different grains. This behavior results in the activation of distinct slip systems, and inevitably leads to slight misorientation of different parts. These parts are separated by dislocation walls or ribbons that are called GNBs. The misorientations of the original GNBs can increase into the typical values of inherent grain boundaries, whereas, the IDBs maintain the level corresponding to the dislocation angle.

The dislocation density of the EPT cold drawing specimen is lower than that of the other specimen, indicating a restriction in the dislocation pile-up under electropulsing treatment. Moreover, the stacking fault energy in the pyramidal  $\langle c+a \rangle$  slip is higher than that of other slip types in Ti–6Al–4V alloy, causing the dislocations easy to cross slips onto the adjacent plane when piling-up at the boundaries, and then gradually become a dislocation cell. The restriction of the pyramidal  $\langle c+a \rangle$  slip under electropulsing conditions consequently restricts the formation of a dislocation cell. The fraction of GNBs is lower in the EPT cold drawing specimen as a result of the better deformation coordination.

The development of the misorientation axis distribution of IDBs is closely related to the activities of the slip systems in the deformed grains. CAMPBELL et al [22] gave a conclusion by comparing in-grain

misorientation axis distribution and Schmid factor of slip system that, when the misorientation axis distribution concentrated around the  $\langle 0001 \rangle$  the grain was mainly deformed by prismatic  $\langle a \rangle$  slip. In addition, the high intensity around  $\langle uv\bar{t}0 \rangle$  (Fig. 12(a)) indicated that the pyramidal  $\langle c+a \rangle$  slip was predominantly activated during the deformation process. After further deformation, IDBs with low misorientations formed gradually because of the dislocation activity. These IDBs can evolve into HAGBs with the angles similar to those of inherent grain boundaries, resulting in high intensity cluster at  $\langle uv\bar{t}0 \rangle$   $20^\circ$ – $30^\circ$ . The maximum value around  $\langle 2\bar{1}\bar{1}0 \rangle$   $30^\circ$ – $40^\circ$  is presented in a previous study. However, the value cannot be explained because of the lacking data analysis framework about the crystallography model of HCP materials [23]. It is supposed to be an approximately random and low energy crystallography orientation statement of deformed Ti–6Al–4V alloy.

## 5 Conclusions

1) High-density electropulsing promotes the deformability of the grains of Ti–6Al–4V alloy with unfavorable orientation. As a result, the deformation microstructure is more homogeneous after EPT cold drawing.

2) During EPT cold drawing, the prismatic  $\langle a \rangle$  slip is promoted by electropulsing, whereas the pyramidal  $\langle c+a \rangle$  slip is restricted. Deformation with  $c$ -component is accommodated by grain boundary sliding.

3) The fraction of LAGBs in the EPT cold drawing sample is lower than that of conventional cold drawing because of the restriction on the formation of IDBs and GNBs under electropulsing.

4) During conventional cold drawing, peaks clustering at  $\langle uv\bar{t}0 \rangle$   $20^\circ$ – $30^\circ$  and  $\langle 2\bar{1}\bar{1}0 \rangle$   $30^\circ$ – $40^\circ$  are observed in the misorientation axis distribution, which indicates the activation of the pyramidal  $\langle c+a \rangle$  slip. But these peaks are absent in the EPT cold drawing.

## References

- [1] BOYER R R. An overview on the use of titanium in the aerospace industry [J]. *Materials Science and Engineering A*, 1996, 213(1–2): 103–114.
- [2] YAMADA M. An overview on the development of titanium alloys for non-aerospace application in Japan [J]. *Materials Science and Engineering A*, 1996, 213(1–2): 8–15.
- [3] PRAKASH D G L, DING R, MOAT R J, JONES I, WITHERS P J, FONSECA J Q D, PREUSS M. Deformation twinning in Ti–6Al–4V during low strain rate deformation to moderate strains at room temperature [J]. *Materials Science and Engineering A*, 2010, 527(21–22): 5734–5744.
- [4] HE D, ZHU J C, ZAEFFERER S, RAABE D, LIU Y, LAI Z L, YANG X W. Influences of deformation strain, strain rate and cooling rate on the Burgers orientation relationship and variants morphology during  $\beta \rightarrow \alpha$  phase transformation in a near  $\alpha$  titanium alloy [J]. *Materials Science and Engineering A*, 2012, 549(6): 20–29.
- [5] CHICHILI D R, RAMESH K T, HEMKER K J. The high-strain-rate response of alpha-titanium: Experiments, deformation mechanisms and modeling [J]. *Acta Materialia*, 1998, 46(3): 1025–1043.
- [6] ZENG Z, JONSSON S, ROVEN H J. The effects of deformation conditions on microstructure and texture of commercially pure Ti [J]. *Acta Materialia*, 2009, 57(19): 5822–5833.
- [7] ZAEFFERER S. A study of active deformation systems in titanium alloys: Dependence on alloy composition and correlation with deformation texture [J]. *Materials Science and Engineering A*, 2003, 344(1–2): 20–30.
- [8] GURAO N P, KAPOOR R, SUWAS S. Deformation behaviour of commercially pure titanium at extreme strain rates [J]. *Acta Materialia*, 2011, 59(9): 3431–3446.
- [9] CONRAD H, YANG D. Influence of an electric field on the plastic deformation of fine-grained MgO at high homologous temperatures [J]. *Acta Materialia*, 2000, 48(16): 4045–4052.
- [10] CONRAD H, YANG D. Effect of an electric field on the plastic deformation kinetics of electrodeposited Cu at low and intermediate temperatures [J]. *Acta Materialia*, 2002, 50(11): 2851–2866.
- [11] CONRAD H. Thermally activated plastic flow of metals and ceramics with an electric field or current [J]. *Materials Science and Engineering A*, 2002, 322(1–2): 100–107.
- [12] GUAN L, TANG G, JIANG Y, CHU P K. Texture evolution in cold-rolled AZ31 magnesium alloy during electropulsing treatment [J]. *Journal of Alloys and Compounds*, 2009, 487(1–2): 309–313.
- [13] HE C S, ZHANG Y D, WANG Y N, ZHAO X, ZUO L, ESLING C. Texture and microstructure development in cold-rolled interstitial free (IF) steel sheet during electric field annealing [J]. *Scripta Materialia*, 2003, 48(6): 737–742.
- [14] SONG Hui, WANG Zhong-jin, GAO Tie-jun. Effect of high density electropulsing treatment on formability of TC4 titanium alloy sheet [J]. *Transactions of Nonferrous Metals Society of China*, 2007, 17(1): 87–92.
- [15] SONG Hui, WANG Zhong-jin. Improvement of mechanical properties of cold-rolled commercially pure Ti sheet by high density electropulsing [J]. *Transactions of Nonferrous Metals Society of China*, 2012, 22(6): 1350–1355.
- [16] VALLE J A, PÉREZ-PRADO M T, RUANO O A. Deformation mechanisms responsible for the high ductility in a Mg AZ31 alloy analyzed by electron backscattered diffraction [J]. *Metallurgical and Materials Transactions A*, 2005, 36(6): 1427–1438.
- [17] WANG X L, WANG Y B, WANG Y M, WANG B Q, GUO J D. Oriented nanotwins induced by electric current pulses in Cu–Zn alloy [J]. *Applied Physics Letters*, 2007, 91(16): 163112–163112-3.
- [18] AGNEW S R, YOO M H, TOMÉ C N. Application of texture simulation to understanding mechanical behavior of Mg and solid solution alloys containing Li or Y [J]. *Acta Materialia*, 2001, 49(20): 4277–4289.
- [19] GUBICZA J, KHOSRAVI E, STOLYAROV V V. Microstructure and thermal stability in CP titanium processed by electroplastic rolling [J]. *Key Engineering Materials*, 2011, 465: 215–218.
- [20] CHUN Y B, BATTAINI M, DAVIES C H J, HWANG S K. Distribution characteristics of in-grain misorientation axes in cold-rolled commercially pure titanium and their correlation with active slip modes [J]. *Metallurgical and Materials Transactions A*, 2010, 41(13): 3473–3487.
- [21] CONRAD H. Effects of electric current on solid state phase transformations in metals [J]. *Materials Science and Engineering A*, 2000, 287(2): 227–237.
- [22] CAMPBELL J, FAHMY Y, CONRAD H. Influence of an electric field on the plastic deformation of fine-grained  $Al_2O_3$  [J]. *Metallurgical and Materials Transactions A*, 1999, 30(11): 2817–2823.
- [23] HU Y, RANDLE V. An electron backscatter diffraction analysis of misorientation distributions in titanium alloys [J]. *Scripta Materialia*, 2007, 56(12): 1051–1054.

## 脉冲电流对 Ti-6Al-4V 冷拉拔变形行为的影响

周 岩, 陈国清, 付雪松, 周文龙

大连理工大学 材料科学与工程学院, 大连 116085

**摘 要:** 利用电子背散射衍射(EBSD)及透射电镜(TEM)研究在脉冲电流作用下 Ti-6Al-4V 钛合金冷拉拔变形后组织及织构的演变。研究表明: 施加脉冲电流可以促进非有利滑移取向的晶粒发生变形, 从而使 Ti-6Al-4V 钛合金各晶粒之间的变形更为协调。常规拉拔和电塑性拉拔的丝材织构对比显示, 脉冲电流促进钛合金柱面 $\langle a \rangle$ 滑移, 抑制锥面 $\langle c+a \rangle$ 滑移, 通过晶界滑移协调  $c$  方向应变。电塑性拉拔钛合金的小角度晶界比例降低, 说明脉冲电流抑制了变形诱发伴生位错晶界和几何必须晶界的形成。

**关键词:** Ti-6Al-4V 合金; 脉冲电流; 冷拉拔; 织构演变

(Edited by Wei-ping CHEN)